Phys Chem Minerals (1988) 16:83–97

PHYSICS AND CHEMISTRY OF MINERALS

Lattice Dynamics and Inelastic Neutron Scattering from Forsterite, Mg_2SiO_4: Phonon Dispersion Relation, Density of States and Specific Heat

K.R. Rao[1], S.L. Chaplot[1], Narayani Choudhury[1], Subrata Ghose[2], J.M. Hastings[3], L.M. Corliss[3], and D.L. Price[4]

[1] Nuclear Physics Division, Bhabha Atomic Research Centre, Trombay, Bombay 400085, India
[2] Mineral Physics Group, Department of Geological Sciences, University of Washington, Seattle, Washington 98195, USA
[3] Chemistry Department, Brookhaven National Laboratory, Upton, New York 11973, USA
[4] Materials Science Division, Argonne National Laboratory, Argonne, Illinois 60439, USA

Abstract. Magnesium-rich olivine $(Mg_{0.9}Fe_{0.1})_2SiO_4$ is considered to be a major constituent of the Earth's upper mantle. Because of its major geophysical importance, the temperature and pressure dependence of its crystal structure, elastic and dielectric constants, long-wavelength phonon modes and specific heat have been measured using a variety of experimental techniques. Theoretical study of lattice dynamics provides a means of analyzing and understanding a host of such experimental data in a unified manner. A detailed study of the lattice dynamics of forsterite, Mg_2SiO_4, has been made using a crystal potential function consisting of Coulombic and short-range terms. Quasiharmonic lattice dynamical calculations based on a rigid molecular-ion model have provided theoretical estimates of elastic constants, long-wavelength modes, phonon dispersion relation for external modes along the three high symmetry directions in the Brillouin zone, total and partial density of states and inelastic neutron scattering cross-sections. The neutron cross-sections were used as guides for the coherent inelastic neutron scattering experiment on a large single crystal using a triple axis spectrometer in the constant Q mode. The observed and predicted phonon dispersion relation show excellent agreement. The inelastically scattered neutron spectra from a powder sample have been analyzed on the basis of a phonon density of states calculated from a rigid-ion model, which includes both external and internal modes. The experimental data from a powder sample show good agreement with the calculated spectra, which include a multiphonon contribution in the incoherent approximation. The computed phonon densities of states are used to calculate the specific heat as a function of temperature using both the rigid molecular-ion and rigid ion models. These results are in very good agreement with the calorimetric measurement of the specific heat. The interatomic potential developed here can be used with some confidence to study physical properties of forsterite as a function of pressure and temperature.

1. Introduction

Magnesium-rich olivine, $(Mg_{0.9}Fe_{0.1})_2SiO_4$, is considered to be the major component of the Earth's upper mantle, whose thermoplasticity is responsible for the movement of the continental plates. The olivine to spinel phase transition at high pressures and temperatures is believed to be responsible for the seismic discontinuity at a depth of 400 Km. Olivine is also a primary condensate of the solar nebula and an important component of the moon, Mercury and the chondritic meteorites. In view of its major geophysical importance, its physical and thermodynamic properties have been investigated by a number of techniques. The elastic constants and their temperature and pressure derivatives have been determined by ultrasonic techniques (Verma 1960; Kumazawa and Anderson 1969; Graham and Barsch 1969; Suzuki et al. 1983). The crystal structure of forsterite, Mg_2SiO_4, at high temperatures and high pressures has been investigated by x-ray diffraction (Smyth and Hazen 1973; Hazen 1976; Takéuchi et al. 1984; Kudoh and Takéuchi 1985). The nature of the electronic charge distribution and chemical bonding has been studied by x-ray diffraction (Fujino et al. 1981; Sasaki et al. 1980, 1982), nuclear magnetic resonance (Derighetti et al. 1978) and quantum mechanical calculations (McLarnan et al. 1979). Dielectric constants and the polarization behavior at high temperatures have been determined by Cygan and Lasaga (1986). Calorimetric measurements of the specific heat of forsterite have been made by Robie et al. (1982). The long-wavelength lattice vibrations have been studied by infrared absorption (IR) and Raman scattering (Paques Ledent and Tarte 1973; Servoin and Piriou 1973; Oehler and Güntherd 1969; Iishi 1978; Jeanloz 1980; Beeson et al. 1982; Hofmeister 1987). A number of studies have been made to computer model the crystal structures, elastic constants, and IR and Raman frequencies of olivine and spinel polymorphs of Mg_2SiO_4 based on a variety of interatomic potentials (Price and Parker 1984; Price et al. 1987; Matsui and Busing 1984).

Most of the physical and thermodynamic properties mentioned above are macroscopic properties representing various kinds of averages over the interatomic forces or correlated atomic vibrations which depend on them. Provided the interatomic forces are properly characterized, these properties and their temperature and pressure derivatives can be calculated from lattice dynamics (see Born and Huang 1954; Brüesch 1982). The interatomic forces can be directly probed by optical techniques (IR, Raman), but they provide information about a limited set of atomic motions, the optically active long-wavelength vibrations (zone center phonons). For a stringent test of the interatomic force model, a knowledge of the phonon dispersion, i.e. the phonon modes throughout the Brillouin zone is necessary. The low-frequency phonon modes and their dispersion are important because they contribute significantly to the low-temperature

specific heat. They can be measured by coherent inelastic neutron scattering from a single crystal because the energy (~25 meV) and wavelength (~1.8 Å) of thermal neutrons from a nuclear reactor are comparable to the phonon energy and interatomic spacings in crystals. Measurement of high-frequency internal modes require higher energy (~200 meV) neutrons from a pulsed spallation source; the frequency spectrum including external and internal modes (generalized density of states) can be measured by the time-of-flight technique on a powder sample.

We have carried out a lattice dynamical calculation of the phonon dispersion relation of the external modes along the three principal directions of the Brillouin zone of forsterite (orthorhombic, space group *Pnma*, 28 atoms in the unit cell) using a rigid-'molecular' ion model (Venkataraman and Sahni 1970), where the $[SiO_4]$ group is assumed to be a rigid unit. This model has been used successfully to calculate phonon dispersion relations for the external modes of α-KNO_3 and $LiKSO_4$ (Rao et al. 1978; Chaplot et al. 1984). The interatomic potential of forsterite consists of a Coulombic and a short-range repulsive term. The calculated phonon dispersion relation and one-phonon dynamic structure factors and their polarizations were used as guides to measure the dispersion of the acoustic and a number of low-lying optic modes in a large single crystal of forsterite using the triple axis spectrometer at the High Flux Beam Reactor at Brookhaven National Laboratory. The generalized phonon density of states, $G(E)$, has been measured using the *Intense Pulsed Neutron Source* (IPNS) at Argonne National Laboratory. $G(E)$ has been derived theoretically from the phonon density of states, $g(\omega)$, calculated from a rigid-ion model, where the rigidity condition has been relaxed and the covalent Si–O interaction has also been taken into consideration. Finally, the specific heat has been calculated from $g(\omega)$ and compared with the calorimetric measurements. The very good agreement between theoretical and experimental results in all three cases indicates that the interatomic force model developed here can be used to predict the physical properties of forsterite and their temperature and pressure dependences with some confidence (Narayani Choudhury et al. 1988).

A computer program DISPR (Chaplot 1978) has been used to compute the phonon frequencies of various wavevectors in the Brillouin zone. The input are the crystal structure, group theoretical symmetry vectors and the optimized crystal potential. The program can also evaluate the phonon density of states, free energy as a function of temperature, specific heat, inelastic neutron cross-section, etc.

The outline of the paper is as follows: The crystal structure of Mg_2SiO_4 is described in Section 2. The group theoretical analysis to classify the lattice modes and their eigenvectors is presented in Section 3 and the nature of the crystal potential and its parameters in Section 4. The experimental results are given in Section 5, followed by a discussion in Section 6 and a summary in Section 7. Short reports of different aspects of this work have appeared earlier (Rao et al. 1985b, 1987; Ghose et al. 1987).

2. Structure

The crystal structure of forsterite Mg_2SiO_4 (Smyth and Hazen 1973; Fujino et al. 1981) consists of isolated $[SiO_4]$ tetrahedra linked by the divalent magnesium cations in six-fold oxygen anion coordination. There are four Mg_2SiO_4 formula units per unit cell and the space group is *Pnma*. The four Mg ions are in two crystallographically distinct positions 4(a) and 4(c), which are designated as M1 and M2 respectively. Silicon atoms reside at 4(c) and the oxygens at position 4(c) (O1 and O2) and 8(d)(O3). The point symmetry of 4(a) is 1, of 4(c) m and of 8(d) $\bar{1}$. The coordination polyhedra around the two non-equivalent six-coordinated magnesium atom positions at M1 and M2 are distorted from regular octahedral symmetry. The M1 octahedron is elongated along the O3–O3 axis whereas the M2 octahedron is slightly irregular. The arrangement of atoms is shown in Figure 1. The structure has mirror planes at $y=1/4$ and $y=3/4$ (parallel to the page in the figure). The discrete SiO_4 tetrahedra have Si, O1, and O2 atoms on the mirror plane and pairs of O3 atoms above and below the mirror in general positions. M1 atoms are situated at the inversion centers and M2 atoms on the mirror planes.

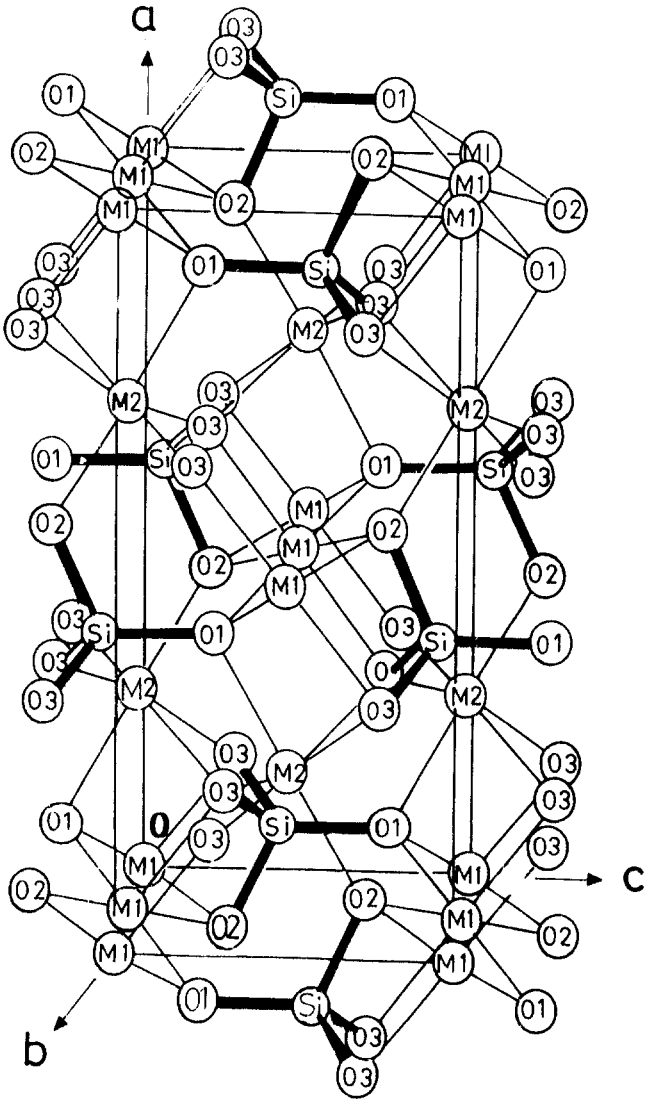

Fig. 1. Crystal Structure of forsterite, Mg_2SiO_4 (Matsui and Busing 1984)

For consistency with the standard space group notation, *Pnma* (D_{2h}^{16}) as given in the International Tables of Crystallography (1952) and for comparison of certain features with the other crystals like α-KNO_3 studied earlier (Rao et al. 1978), we have adopted the crystal structure information

Table 1. Lattice constants, fractional Coordinates and labelling of atoms and 'molecules' in the unit cell. Orthorhombic space group *Pnma* $Z=4$. $a=10.1902$, $b=5.9783$, $c=4.7534$ Å

Atom	X	Y	Z	Atom label	Molecule label
MgI	0.00000	0.00000	0.00000	1	1
MgI	0.50000	0.50000	0.50000	2	2
MgI	0.00000	0.50000	0.00000	3	3
MgI	0.50000	0.00000	0.50000	4	4
MgII	0.27740	0.25000	−0.00830	5	5
MgII	0.77740	0.25000	0.50830	6	6
MgII	0.72260	0.75000	0.00830	7	7
MgII	0.22260	0.75000	0.49170	8	8
Si	0.09400	0.25000	0.42650	9	
O1	0.09160	0.25000	0.76590	10	
O2	−0.05290	0.25000	0.27840	11	9
O3	0.16310	0.03300	0.27750	12	
O4	0.16310	0.46700	0.27750	13	
Si	0.59400	0.25000	0.07350	14	
O1	0.59160	0.25000	−0.26590	15	
O2	0.44710	0.25000	0.22160	16	10
O3	0.66310	0.46700	0.22250	17	
O4	0.66310	0.03300	0.22250	18	
Si	−0.09400	0.75000	0.57350	19	
O1	−0.09160	0.75000	0.23410	20	
O2	0.05290	0.75000	0.72160	21	11
O3	−0.16310	0.53300	0.72250	22	
O4	−0.16310	0.96700	0.72250	23	
Si	0.40600	0.75000	−0.07350	24	
O1	0.40840	0.75000	0.26590	25	
O2	0.55290	0.75000	−0.22160	26	12
O3	0.33690	0.96700	−0.22250	27	
O4	0.33690	0.53300	−0.22250	28	

given in Table 1. The space group operations of *Pnma* are given in Table 2.

3. Group Theoretical Analysis of Lattice Modes of Mg_2SiO_4

Maradudin and Vosko (1968) have outlined the method of group theoretical analysis of lattice vibrations of crystals making use of Irreducible Multiplier Representations. The scheme for group theoretical analysis of the external modes in crystals containing atoms and rigid 'molecules' is given by Venkataraman and Sahni (1970). Sieskind (1978) discussed how one can simplify the evaluation of group theoretical information making use of the *Group of Neutral Elements of crystal Sites* (GNES). This elegant method has been extended to cover the study of crystals containing atoms and 'molecules' (Rao et al. 1982). The GNES is used to analyse the symmetry aspects of lattice modes in Mg_2SiO_4.

We have studied the phonon dispersion relation along the three symmetry directions, Σ, Λ and Δ. The group of the wavevectors and their representations along these three directions are given in Table 3. There are no degenerate branches along any of the three directions. The symmetry vectors of normal vibrations along the three symmetry directions and at $q=0$ are derived using the method of Rao et al. (1982). These symmetry vectors, given in the Appendix, have been used in block diagonalising the dynamical matrix, representation by representation, and for checking other aspects of the numerical evaluations. The symmetry vectors are also useful in visualising the nature of the atomic vibrations for various modes. However, the eigenvectors associated with normal modes could be linear combinations of the symmetry vectors that belong to a particular representation.

Table 3. Group of wavevectors along Σ, Δ and Λ directions and their irreducible representations

$\Sigma(\xi,0,0)$	$G_0(\Sigma)$:	$R1$	$R2$	$R7$	$R8$
$\Delta(0,\xi,0)$	$G_0(\Delta)$:	$R1$	$R3$	$R6$	$R8$
$\Lambda(0,0,\xi)$	$G_0(\Lambda)$:	$R1$	$R4$	$R6$	$R7$
Representation					
$\Sigma1\,\Delta1\,\Lambda1$		1	1	1	1
$\Sigma2\,\Delta2\,\Lambda2$		1	1	−1	−1
$\Sigma3\,\Delta3\,\Lambda3$		1	−1	1	−1
$\Sigma4\,\Delta4\,\Lambda4$		1	−1	−1	1

$R1$, $R2$ etc. are the point group operations associated with the space group operations $S1$, $S2$ etc. given in Table 2

4. Lattice Dynamical Calculations

4.1. *Potential Function for* Mg_2SiO_4

The lattice dynamical calculations are carried out corresponding to both the rigid molecular-ion model and the rigid ion model. In the rigid molecular-ion model the magnesium ions are associated with translational degrees of freedom whereas the silicate groups are assumed to be rigid units capable of translations and rotations only; this model helps to identify the rotational modes and their eigenvectors easily. In the rigid ion model, on the other hand, each ion is treated independently; since each ion is associated with translational degrees of freedom in this model, the internal vibrations of silicates also are considered in detail in this model. [For details of these two models, see Venkataraman

Table 2. Space group operations of Mg_2SiO_4 (*Pnma*)

Space group operation	$S1$	$S2$	$S3$	$S4$	$S5$	$S6$	$S7$	$S8$
In Seitz's notation	$\{E/O\}$	$\{C_2(x)/V_1\}$	$\{C_2(y)/V_2\}$	$\{C_2(z)/V_3\}$	$\{i/O\}$	$\{\sigma_2(x)/V_1\}$	$\{\sigma_2(y)/V_2\}$	$\{\sigma_2(z)/V_3\}$
International Tables	(xyz)	$(x-y-z/V_1)$	$(-xy-z/V_1)$	$(-x-yz/V_3)$	$(-x-y-z)$	$(-xyz/V_1)$	$(x-yz/V_2)$	$(xy-z/V_3)$

$V_1=(1/2\ 1/2\ 1/2)$; $V_2=(0\ 1/2\ 0)$; $V_3=(1/2\ 0\ 1/2)$

and Sahni (1970), Rao et al. (1978), and Venkataraman et al. (1975).]

The form of the interatomic potential function chosen to describe the interaction between two non-bonded atoms k in 'molecule' K denoted as (Kk) and the atom k' in 'molecule' K' denoted as $(K'k')$ separated by a distance r is given by,

$$V(r)=\frac{e^2}{4\pi\varepsilon_0}\frac{Z(Kk)\,Z(K'k')}{r}+a\exp\left\{-\frac{br}{R(Kk)+R(K'k')}\right\} \tag{1}$$

where $1/(4\pi\varepsilon_0)=9.0\times10^9$ nt-m^2/coul^2. As a result of study of a large number of complex crystals (see Rao and Chaplot (1985c) and references cited therein), we find that values of a equal to 1822 eV and b equal to 12.364 are appropriate in all these systems. The choice of these constants has been discussed by Rao et al. (1978). $Z(Kk)$ and $R(Kk)$ are the fractional charge and radius parameters associated with atom k belonging to the rigid unit K. The radius parameters are scaled from Shannon's crystal radii. This form of the potential function is the simplest one with a minimum number of parameters to use in the study of the dynamics of complex ionic 'molecular' solids like Mg_2SiO_4.

After the form of the potential was chosen, the following criteria governed the optimisation of the parameters of the potential:

(i) lattice constants and atomic positions should correspond to the experimentally determined structure;

(ii) the ionic charges and radius parameters should be close to those derived from x-ray diffraction studies;

(iii) the forces on the atoms and molecules and torques on molecules must vanish;

(iv) the internal stresses due to the chosen unit cell and atomic parameters should be minimum;

(v) the eigenvalues must be positive;

(vi) the calculated elastic constants should agree with the experimental values within reasonable limits; the long-wavelength optic modes should span the range of experimental observations from Raman and infrared spectra.

There are two sets of interatomic potential parameters available for computations: (a) those determined by Iishi (1978) on the basis of IR and Raman data and (b) those arrived at through x-ray diffraction data analysis by Fujino et al. (1981). Iishi (1978) has studied the IR and Raman data on the basis of a purely *short range* (SR) model, a *rigid ion* (RI) model and a *polarisable ion* (PI) model. The force constants were fitted to reproduce the experimental $q=0$ mode frequencies. His rigid ion and polarisable ion models explained reasonably well the LO−TO splittings. However, his charge parameters when used in our rigid molecular-ion model yielded elastic constants which were one order of magnitude less than the experimental values; the agreement with the optic data was also rather poor. His charge parameters were found to be roughly 60 percent of our final optimised charge parameters.

We, therefore, resorted to a second computation with the charge parameters given by Fujino et al. (1981). Fujino et al. have determined the net atomic charges from the electron density distribution by direct integration of the electron density within the sphere of a newly defined radius, the *Effective Distribution Radius* (EDR) for each cation. Their results for Mg_2SiO_4 are given in Table 4 under Model II. Using this set of charge parameters, we again optimised the short-range parameters on the basis of minimizing forces and torques in the system. The values for the elastic constants improved although there were some residual forces on all the atoms. Also the pressure on the system was quite large ($\approx$15 GPa). At this stage, the charges were lowered by about 10 percent from Fujino's values and the charges and radii of MgI and MgII were varied individually. The pressure was down to 1 GPa. However, in order to reduce the torque on SiO_4, the group had to be rotated by about 0.3 degree. In Table 4 the optimised potential parameters are given under Model III; this set of parameters has been used in all the calculations. With these changes the following observations were made:

Table 4. Effective charges and radii used in lattice dynamical computations

	Mg(1)	Mg(2)	Si	O(1)	O(2)	O(3) & O(4)
Model I						
Iishi (1978)						
Charges	0.93	0.93	0.7	−0.63	−0.63	−0.63
Radii	0.96	0.96	0.685	0.960	0.960	0.960
Model II						
Fujino et al. (1981)						
Charges	1.76	1.74	2.11	−1.52	−1.29	−1.40
Radii (EDR)	0.93	0.93	0.94	0.96	0.96	0.96
Model III						
This work-optimum parameters						
Charges	1.60	1.80	1.0	−1.2	−1.0	−1.10
Radii	1.68	1.73	1.0	1.55	1.45	1.50

(a) the pressure on the system is quite low, equal to 0.4 GPa;

(b) the comparison of elastic constants as calculated with experimental data is fair (see Table 5);

(c) the long-wavelength optic modes span the range of the experimental data from IR and Raman spectroscopies (see Tables 6 and 7);

(d) the forces and torques on the constituents of the unit cell are quite small although non-vanishing

(e) the cohesive energy is reasonable, equal to −245 ev/unit cell;

and

(f) all eigenvalues are positive.

As already stated, in the rigid ion model, in addition to the external degrees of freedom, the internal degrees of freedom are also accounted for. The silicate group, in this model, is no longer rigid; we allow for Si−O and O−O interactions in the silicate groups. The Si−O bond stretching potential is taken to be of the form

$$V(r_{\mathrm{Si-O}})=-CD\exp\left\{-\frac{n}{2C}\frac{(r_{\mathrm{Si-O}}-r_0)^2}{r_{\mathrm{Si-O}}}\right\} \tag{2}$$

with parameters C, D, n and r_0. In order to simulate the O−Si−O bond bending potential, we have assumed an O−O interaction of the following form for any two oxygen atoms of the same silicate unit, as in our earlier work on $LiKSO_4$:

$$V(r_{O-O})=\frac{e^2}{4\pi\varepsilon_0}\frac{Z^2(O)}{r_{O-O}}+sa\exp\left\{\frac{-br_{O-O}}{2R(O)}\right\}-\frac{w}{r_{O-O}^6} \quad (3)$$

with parameters s and w. The parameters $Z(O)$, $R(O)$, a and b were identical with the optimum parameters chosen in the rigid molecular-ion model. The parameters C, D, n, r_0, s and w were optimised to reproduce the experimental long-wavelength data. The final set of parameters is $C=1$, $D=3.4$ eV, $n=10.5$ Å^{-1}, $r_0=1.61$ A, $s=55$ and $w=1250$ eV Å^6.

The dynamical equations given in Section 6 of Rao et al. (1978) have been used along with the potential discussed above to derive the phonon frequencies and eigenvectors. The programme DISPR (Chaplot 1978) has been used in the numerical computations.

5. Experimental

Raman and infrared spectroscopies provide somewhat limited information on lattice dynamics as they are probes for studying only the long-wavelength modes; they are also restricted by certain selection rules which may not permit probing all long-wavelength modes. In principle, coherent inelastic neutron scattering techniques allow us to probe all the normal modes across the Brillouin zone. Two types of experiments can be carried out using the techniques of neutron scattering: by analysing the energy of the scattered neutrons, (i) from a polycrystalline sample over a wide angular range, one can measure the one-phonon density of states, and (ii) from a single crystal, one can measure the phonon dispersion curves along specific directions in $Q-\omega$ space. The one-phonon density of states as well as the phonon dispersion curves can be used to test the validity of the model calculations. We have carried out both of these experiments on $\alpha-Mg_2SiO_4$.

5.1. Inelastic Neutron Scattering from Polycrystalline Mg_2SiO_4, Phonon Density of States

The *Low Resolution Medium Energy Chopper Spectrometer* (LRMECS) at the *Intense Pulsed Neutron Source* (IPNS), Argonne National Laboratory, was used for measuring the inelastic neutron spectra from a powder sample of Mg_2SiO_4 by the time-of-flight method. Figure 2 gives the schematic layout of LRMECS. The chopper has a body of beryllium with aluminium end-caps; a boron fiber/aluminium composite defines the slits. A suitable electronic control system maintains the chopper in a fixed phase relative to the accelerator source. Approximately 100 ^{3}He proportional counters detect scattered neutrons. The signals are processed by the IPNS Data Acquisition System and the data are analysed on the VAX 11-780 computer using general purpose programs (Price 1982). The analysis consists of converting the data from the sample into the scattering function $S(\phi, E)$ (ϕ-scattering angle, E-energy loss of scattered neutrons) after correcting for background and contribution from the empty sample container. $S(\phi, E)$ is obtained on an absolute scale by comparing with standard vanadium data and taking into account the efficiency function of the detectors. In order to compare with theory, one can convert $S(\phi, E)$ to $S(Q, E)$, Q being the momentum transfer from the neutrons to the sample in the scattering process, and apply suitable corrections for energy and momentum resolution. 160 detector inputs were grouped into 42 detector subgroups in the range of scattering angle $-10°$ to 116.4°. The sample transmission was 91.1 percent at the incident neutron energy of 200.0 meV. The nominal sample temperatures in two sets of experiments were 14 K and 300 K. The large incident energy helped to cover the full range of one-phonon modes with a Q-range of about 6–13 Å^{-1}. The energy transfer and wavevector transfer resolution were approximately 12 meV and 0.5 Å^{-1}.

Coherent inelastic neutron scattering measures the scattering function in terms of Q and E which in the conventional harmonic phonon expansion can be written as (Carpenter and Price 1985)

$$S(\boldsymbol{Q}, E)=S^{(0)}+S^{(1)}+S^{(m)}. \quad (4)$$

$S^{(0)}$, $S^{(1)}$ and $S^{(m)}$ represent elastic, one-phonon and multi-phonon scattering. $S^{(0)}$ and $S^{(1)}$ are given by

$$S^{(0)}(\boldsymbol{Q}, E)=\frac{1}{N}\sum_{ij}\frac{b_i b_j}{\langle b^2\rangle}\exp\{-(W_i+W_j)\}\exp\{i\boldsymbol{Q}\cdot(\boldsymbol{R}_i-\boldsymbol{R}_j)\} \quad (5a)$$

$$S^{(1)}(\boldsymbol{Q}, E)=\frac{1}{N}\sum_{ij}\frac{b_i b_j}{\langle b^2\rangle}\exp\{-(W_i+W_j)\}\exp\{i\boldsymbol{Q}\cdot(\boldsymbol{R}_i-\boldsymbol{R}_j)\}\times\sum_l\frac{\hbar(\boldsymbol{Q}\cdot\boldsymbol{\xi}_i^l)(\boldsymbol{Q}\cdot\boldsymbol{\xi}_j^l)}{\omega_l\sqrt{M_i M_j}}(n_l+1)\,\delta(E-\hbar\omega_l). \quad (5b)$$

Expression (5b) is for neutron-energy-loss processes. Here W_i is the Debye-Waller factor and M_i the nuclear mass associated with atom of species i, $\boldsymbol{R}_i$ its equilibrium position, b_i its scattering length, and $\boldsymbol{\xi}_i^l, \omega_l$ and $n_l=\{\exp(\hbar\omega_l/kT)-1\}^{-1}$ are the displacement vector, frequency and population factor of the normal mode l. In the incoherent approximation, one assumes that, when $S(\boldsymbol{Q}, E)$ is averaged over an extended range of $\boldsymbol{Q}$, the correlation between motions of different atoms dies out and the factors $(\boldsymbol{Q}\cdot\boldsymbol{\xi}_i^l)$ $(\boldsymbol{Q}\cdot\boldsymbol{\xi}_j^l)$ may be replaced by $\frac{1}{2}Q^2(\xi_i^l)^2\delta_{ij}$. In this case Eq. (5b) takes the much simpler form

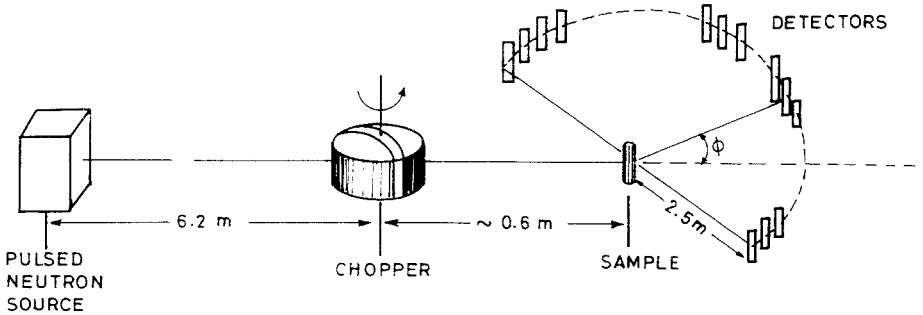

Fig. 2. Schematic layout of Low Resolution Medium Energy Chopper Spectrometer (LRMECS)

$$S_{\text{inc}}^{(1)}(\boldsymbol{Q}, E)=\sum_i \frac{b_i^2}{\langle b^2\rangle} e^{-2W_i} \frac{Q^2}{2M_i} \frac{g_i(\omega)}{E=\hbar\omega}(n+1) \qquad (6)$$

where $g_i(\omega)$ is the displacement weighted density of states for atoms of type i.

5.2. *Inelastic Neutron Scattering from Single Crystal Forsterite, Phonon Dispersion Relation*

The medium-resolution, medium-energy, triple-axis spectrometer at Brookhaven National Laboratory was used for measuring the phonon dispersion curves along high symmetry directions of Mg_2SiO_4. A synthetic forsterite crystal of dimensions $3\times1\times1$ cm^3, kindly made available by Prof. H. Takei of Tokyo University, Japan, was used in these experiments. The sample temperature was near 300 K. A germanium (111) monochromator with a mosaic spread of nearly 12 min and a pyrolytic graphite (004) analyser were used for the measurements. The collimation between the reactor and monochromator, monochromator and sample, sample and analyser, and analyser and detector were 20′, 20′, 20′, 40′ in most of the measurements. The collimation between the monochromator and the sample was removed in a few measurements which resulted in doubling the neutron intensity. Incident neutron energies were fixed at either 45.303 meV or 60.00 meV in these experiments. The measured phonon groups were normalised to monitor settings varying from 400 to 10000 neutron counts. It took approximately 16.5 min per point of neutron group at a monitor setting of 10000 counts.

5.3. *One-phonon Cross-Section*

The calculation of the lattice dynamics of Mg_2SiO_4 discussed above helped to plan the coherent inelastic neutron scattering experiments from the single crystal. We evaluated the one-phonon neutron cross section for scattering from a single crystal for each mode in two of the three mutually perpendicular planes of the reciprocal space namely, in the planes $(hk0)$, $(h0l)$ and $(0kl)$. The wavevector transfer lies in the range of $Q=0$ to 8 Å^{-1}. These results, available in the form of tables for each mode around various reciprocal lattice vectors, were used as guides in the choice of reciprocal space regions in which to measure the modes. From the actual measurements one could ascertain the mode frequencies.

Figure 3 shows a few of the typical neutron groups from these experiments.

6. Results and Discussion

6.1. *Phonon Dispersion Curves along High Symmetry Directions and Elastic Constants*

Having optimised the potential on the basis of the criteria given in section 4, the group theoretical information given in section 3 was used in diagonalising the dynamical matrix for wavevectors along the three high symmetry directions and in classifying the normal modes that belong to different representations. As already stated, program DISPR has been used in all these computations. The acoustic modes

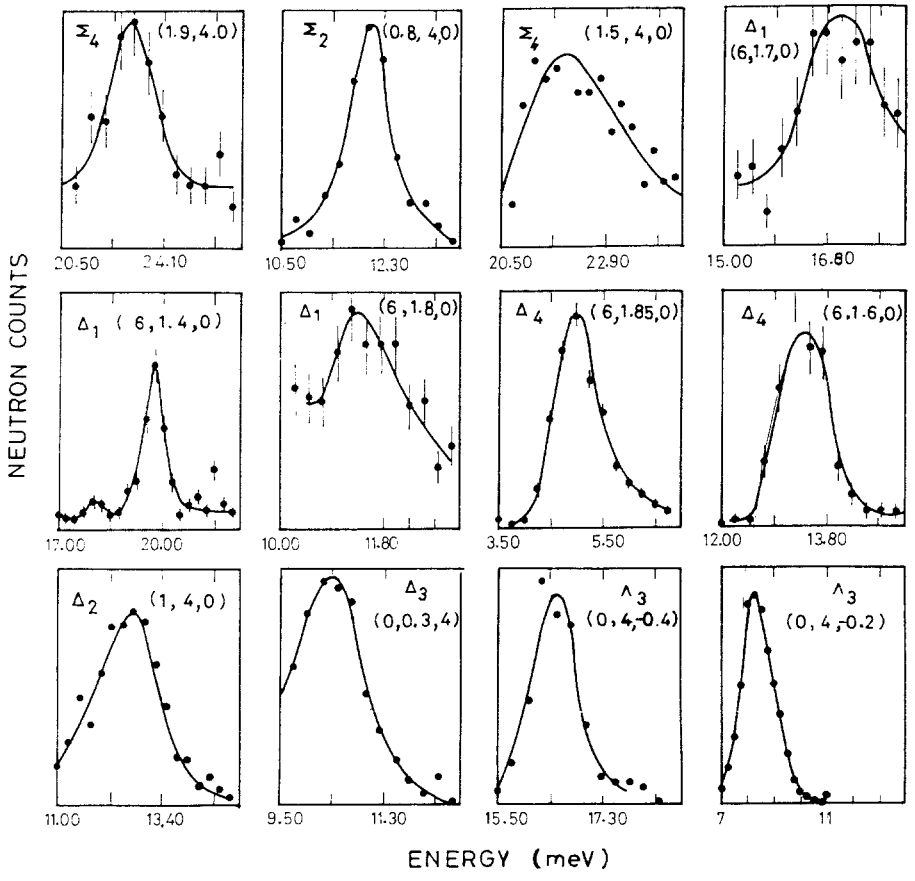

Fig. 3. Typical neutron groups associated with phonons from a single crystal of Mg_2SiO_4. The representations to which the phonons belong are indicated by greek letters. The numbers in parentheses indicate the coordinates of the wavevector transferred in the neutron scattering process in units of reciprocal lattice vectors. The ordinate is in arbitrary units as the neutrons are counted for varying periods of time

Table 5. Comparison of theoretical and experimental elastic constants (10^{10} dynes/cm^2)

	Experimental			Theoretical	
	Graham et al. (1969)	Kumazawa et al. (1969)	Suzuki et al. (1983)	Iishi (1978)	Present work[a]
C_{11}	200.5	199.5	199.8	215.7	194.6
C_{22}	236.3	235.3	235.5	207.2	235.0
C_{33}	329.1	328.4	328.7	273.4	279.2
C_{44}	81.1	80.82	80.57	74.4	94.2
C_{55}	81.4	81.2	80.95	74.5	80.6
C_{66}	67.2	65.15	66.78	71.6	76.1
C_{12}	72.8	73.8	72.7	86.1	79.0
C_{13}	66.3	63.9	66.7	91.8	71.0
C_{23}	68.4	68.8	68.4	78.4	76.0

[a] Calculated from the slopes of acoustic phonons in the rigid molecular-ion model; since the values obtained from the slopes of the relevent TA branches along different directions were slightly different, average values are presented here for C_{44}, C_{55}, C_{66}

are used to determine the elastic constants in the long-wavelength limit and comparison of these with the experimental data is given in Table 5. The agreement is good, with discrepancies on the order of 10 percent. Theoretical phonon dispersion curves were obtained along the three symmetry directions Σ, Δ and Λ (Fig. 4). The modes that belong to different representations are plotted separately in this figure.

A comparision of results of the coherent inelastic neutron scattering experiments from the single crystal with the theoretical results is shown in Figure 5. Experimental data permit us to make the comparision up to energies of the order of 25 meV. The agreement between experimental data and theoretical predictions is quite satisfactory. A comparison of neutron group intensities associated with each phonon mode with the calculated one-phonon cross section (with suitable scaling factors) indicates that the agreement between the two is good, with an R-factor of nearly 0.3 without any fitting. This leads us to believe that the model with

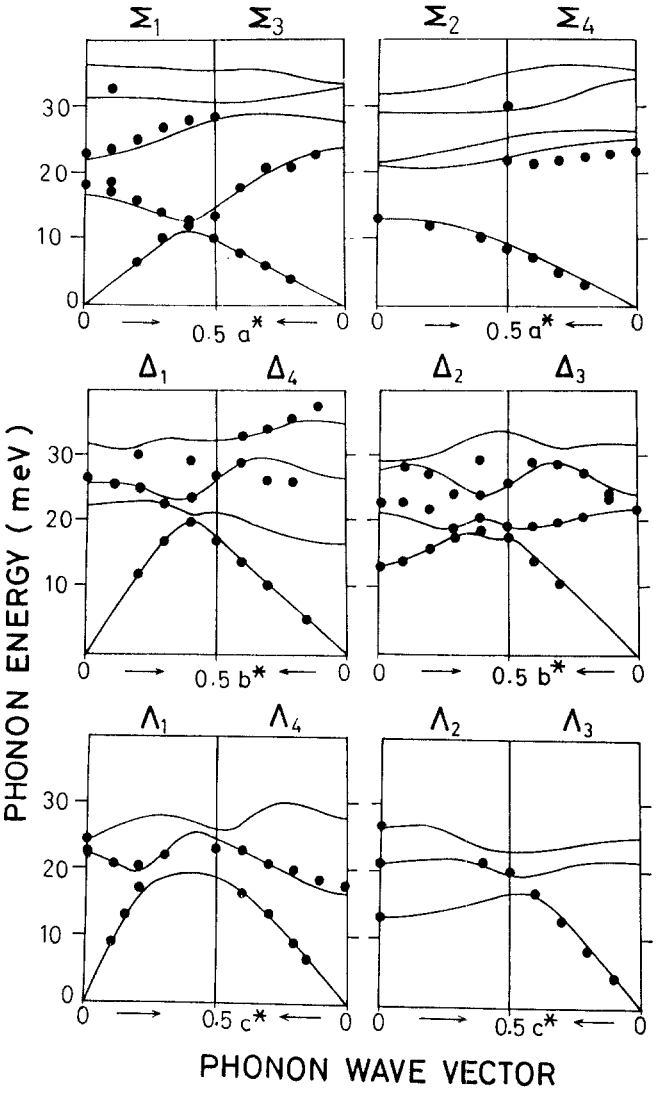

Fig. 5. Comparison of experimental and theoretical phonon dispersion curves; continuous lines are from theory, full circles are experimental values. The theoretical curves are *not* fitted to experimental data but were *predictions* before the experiments were conducted

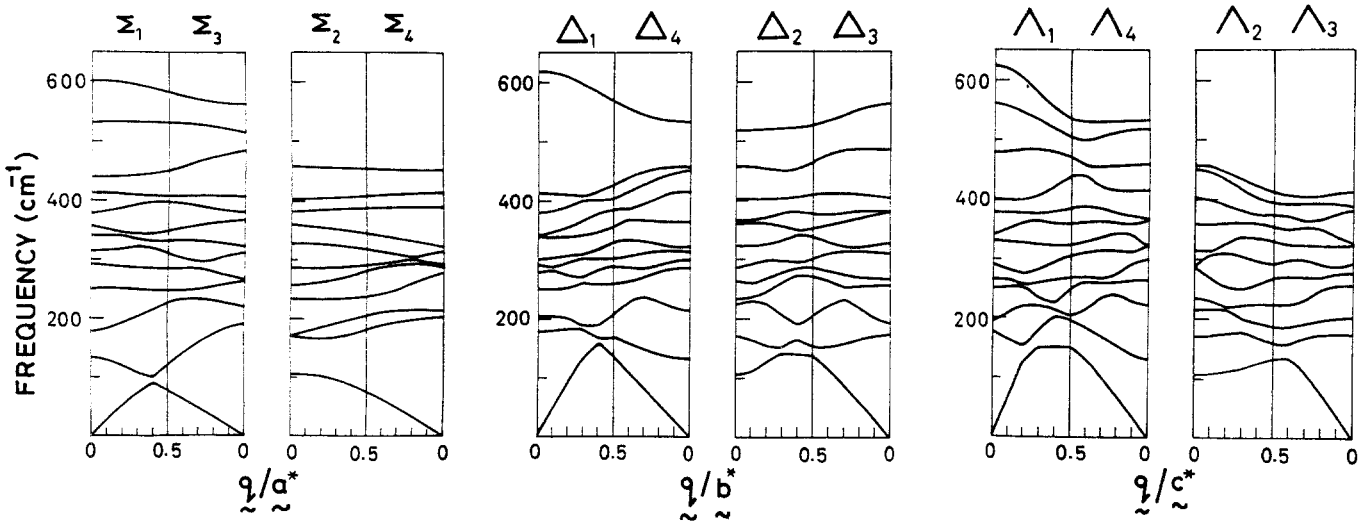

Fig. 4. Theoretical phonon dispersion relation of Mg_2SiO_4 in external mode formalism. The figures are drawn in extended zone scheme for easy visualisation; group theoretical representations are indicated on top of the figure

its associated parameters is quite acceptable for further detailed studies.

6.2. Phonon Density of States

The phonon density of states gives us an overall view of the range and the extent of various phonon modes in the lattice. Detailed evaluation of the partial density of states in the lattice is useful in (i) understanding the dynamical aspects related to the translation of each atom and the translation and rotation of each rigid group and (ii) evaluating the neutron cross-sections.

The phonon density of states $g(\omega)$ is defined by

$$g(\omega)=A\int_{BZ}\sum_{j}\delta\{\omega-\omega_j(\boldsymbol{q})\}\,\mathrm{d}\,\boldsymbol{q}=A\sum_{jp}\delta\{\omega-\omega_j(\boldsymbol{q})\}\,\mathrm{d}\,\boldsymbol{q}_p \qquad (7)$$

where A is a normalisation constant such that $\int g(\omega)\,\mathrm{d}\,\omega=1$, $\omega_j(\boldsymbol{q})$ is the phonon frequency of the j^{th} normal mode of phonon of wave vector $\boldsymbol{q}$, p is the mesh index in the discretised *Irreducible Brillouin Zone* (IBZ) and $\delta\boldsymbol{q}_p$ provides the weighting factor corresponding to the volume of the p^{th} mesh in $\boldsymbol{q}$-space. Space group symmetry allows the numerical evaluations to be confined to wavevectors within the IBZ. Root sampling method is used in obtaining $g(\omega)$ and histograms of $g(\omega)$ at intervals of $\Delta\omega=2\ \mathrm{cm}^{-1}$ are plotted. Detailed computations were carried out corresponding to the rigid molecular-ion model, sampling 125 wave vectors to obtain the density of states shown in Figure 6. Subsequently, the density of states appropriate to the rigid ion model were also obtained in a much coarser mesh, sampling 27 wave vectors in the IBZ. The density of states shown in Figure 8 at energies above the external mode region are identifiable with the internal modes of SiO_4. The density of states based on the rigid ion model was used in determining the neutron intensity distribution expected from a powder as well as to evaluate the specific heat as a function of temperature.

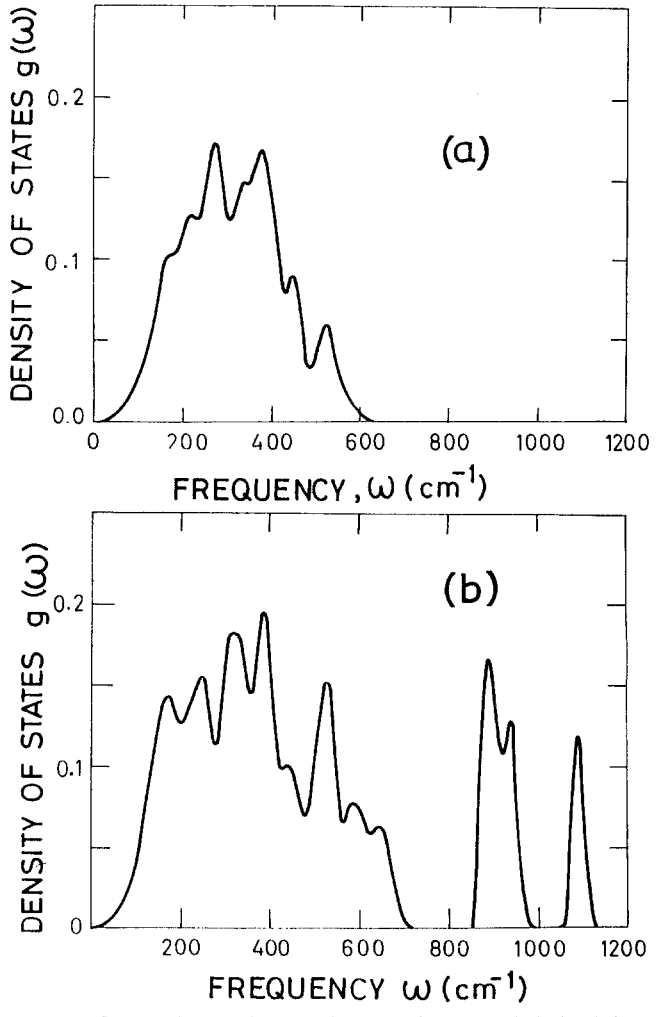

Fig. 6a, b. Total one-phonon density of states (**a**) derived from the rigid molecular-ion model; (**b**) derived from the rigid ion model. The density of states is smoothened with a Gaussian with FWHM of 4 meV

6.3. Partial Density of States and Neutron Intensity Distribution from a Powder

Corresponding to the 48 degrees of freedom of external modes per unit cell in Mg_2SiO_4, there are 48 phonon modes (j is the mode index) for any wavevector $\boldsymbol{q}$ and there are 48 eigenvector components associated with each one of the 48 modes. The eigenvector $\xi^i_{jn/m}(\boldsymbol{q})$ contains detailed information about the displacement components for each of the atoms and the molecules; the translational and rotational displacements of molecules are identifiable separately. The eigenvector $\xi_j(\boldsymbol{q})$ is, therefore, a direct sum of the mass weighted (moment-of-inertia-weighted, for rotational displacements) partial eigenvectors $\xi^i_{jn/m}(\boldsymbol{q})$ of the atoms and molecules, that is,

$$\xi_j(\boldsymbol{q})=\sum_{nm}\{\xi^T_{jn}(\boldsymbol{q})\oplus\xi^T_{jm}\oplus\xi^R_{jm}(\boldsymbol{q})\}. \qquad (8)$$

Here n and m are the atomic and molecular indices, T and R represent translational and rotational components. Each partial eigenvector is a 3-dimensional vector consisting of translational or rotational displacement components along the cartesian axes.

The partial density of states $g^{T/R}(\omega)$ associated with each of the partial eigenvectors is defined by the relation

$$g^{T/r}_{n/m}(\omega)=A\sum_{\text{unit cell}}\sum_{jp}\delta\{\omega-\omega_j(\boldsymbol{q}_p)\}\,|\xi^{T/R}_{j,n/m,\alpha}(\boldsymbol{q}_p)|^2\,\mathrm{d}\,\boldsymbol{q}_p. \qquad (9)$$

$\sum_{\text{unit cell}}$ indicates that the summation is carried out over all the atoms or molecules of the same i^{th} species in the unit cell. The partial density of states in the rigid molecular-ion model is shown in Figure 7.

The computation of the neutron intensity distribution scattered from a powder involves estimation of the multiphonon contribution for comparison with experimental data. However, for coherently scattering samples, estimation of the multiphonon scattering taking into account interference effects in all orders has not been attempted so far. Instead, one resorts to what is referred to as the incoherent approximation, where one neglects the interference effects. $S^{(m)}$ in this approximation is given by

$$S^{(m)}(\boldsymbol{Q},E)=\sum_i\frac{A_i}{M_i}S^{(m)}_i(\boldsymbol{Q},E) \qquad (10)$$

where the total multiphonon scattering is assumed to be a sum of partial multiphonon scattering from each species

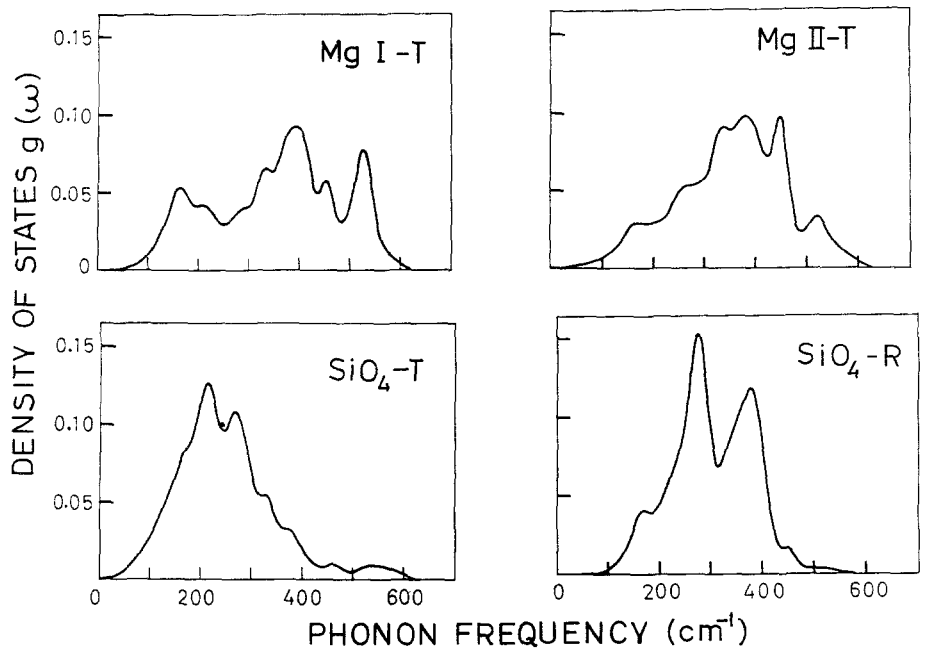

Fig. 7. Partial phonon density of states of Mg_2SiO_4 in the rigid molecular-ion model. The partial densities of states corresponding to translational modes of magnesium ions, silicate 'molecules' and rotations of silicate 'molecules' are shown separately. The densities of states are smoothened with a Gaussian with FWHM of 4 meV

of atoms weighted independently with the corresponding total scattering cross-sections. The computation of $S_i^{(m)}(\boldsymbol{Q}, \omega)$ is carried out assuming Sjolander's formalism (1958). $S_i^{(m)}(\boldsymbol{Q}, \omega)$ is given by

$$S_i^{(m)}(\boldsymbol{Q}, \omega) = e^{-2W_i} \sum_{n=2}^{\infty} G_n(\omega) \frac{(2W_i)^n}{n!} \tag{11}$$

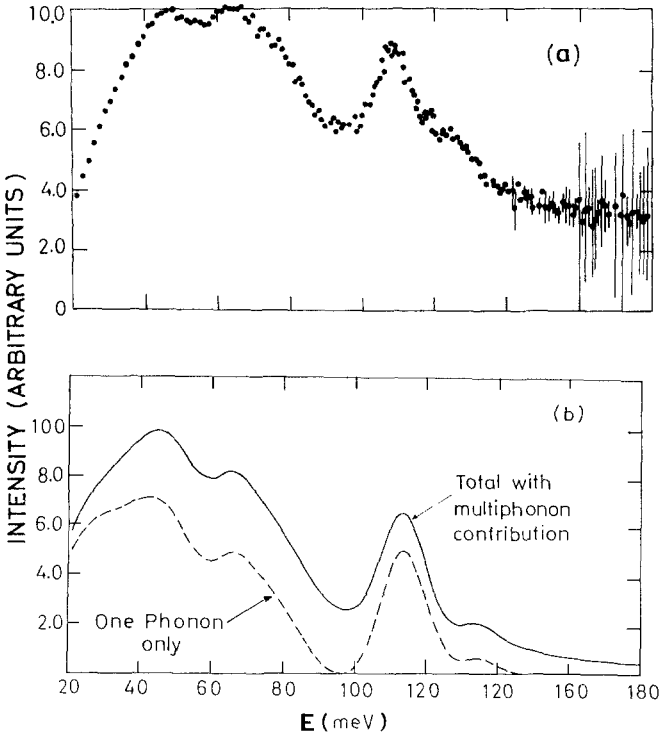

Fig. 8a, b. Comparison of the inelastic neutron spectrum from a powder with the calculated spectrum based on the rigid ion model (**a**) experimentally derived spectrum at 300 K; (**b**) theoretically evaluated spectrum including multiphonon contribution broadened by resolution (FWHM 12 meV) and its one phonon component broadened by the same resolution

with

$$G_0(\omega) = \delta(\omega); \quad G_1(\omega) = g(\omega), \tag{12}$$

the partial density of states, and

$$G_n(\omega) = \int_{-\infty}^{\infty} g_i(\omega - \omega') G_{n-1}(\omega') \, d\omega' \tag{13}$$

giving the higher order terms. It may be noted that the elastic and one-phonon terms are excluded from the summation as they are explicitly taken into account as $S^{(0)}$ and $S^{(1)}$ in Equation (4) earlier. However if the terms corresponding to n equal to 0 and 1 are also evaluated, then the total scattering is automatically obtained.

Figure 8 shows the comparison of the calculated neutron spectrum taking into account the one-phonon and multiphonon contributions as outlined above with the experimental neutron spectrum at 300 K. The comparison is quite good in view of the assumptions made and helps us to understand the observed spectrum. The calculated intensity has been broadened with a uniform instrumental resolution of 12 meV.

6.4. Comparison of Computed Long Wavelength Modes and LO – TO Mode Frequencies with Experimental Data (external modes only)

The optical data of forsterite has been determined by polarised infrared and Raman spectroscopies (Iishi 1978). A comparison of our calculated $\boldsymbol{q} \approx 0$ mode frequencies with experimental data along with our calculated eigenvector components corresponding to translations of MgI and MgII atoms, SiO_4 groups and rotations of $[SiO_4]$ groups is given in Table 6 and 7.

From the group theoretical symmetry vectors or calculated polarisation vectors, one observes that the Γ_1, Γ_2, Γ_3, Γ_4 and Γ_5 representations involve only nonpolar modes which do not exhibit any LO – TO splitting. These nonpolar modes obtained in the rigid molecular-ion model are compared with optical data in Table 6. It can be seen that for

Table 6. Non-polar long-wavelength modes in Mg_2SiO_4

Repn.	Phonon frequency (cm^{-1})			Phonon eigenvector				
	Exptl.	Iishi (1978)	This work	Iishi (1978)	This work (eigenvector[2] [a])			
					MgI T	MgII T	SiO_4 T	SiO_4 R
$\Gamma_1(A_g)$	340	358	380	$R(SiO_4, z)$	0	0.83	0.09	0.08
	329	288	342	T(MgII, y)	0	0.44	0.10	0.46
	305	269	293	T(MgII, SiO_4, x)	0	0.26	0.36	0.38
	227	225	252	$T(SiO_4$, MgII, y)	0	0.09	0.90	0.01
	183	157	178	T(MgII, SiO_4, x)	0	0.32	0.59	0.09
$\Gamma_2(A_u)$	silent		458		0.15	0.67	0.03	0.15
			403		0.62	0.01	0.09	0.28
			359		0.47	0	0.06	0.47
			286		0.78	0.02	0.04	0.16
			233		0.19	0.15	0.08	0.58
			170		0.34	0.07	0.31	0.28
			105		0.45	0.08	0.40	0.07
$\Gamma_5(B_{1g})$	368	362	452	$R(SiO_4, y)$	0	0.71	0.03	0.26
	324	306	314	$R(SiO_4, x)$	0	0.03	0.58	0.39
	244	267	288	$T(SiO_4, z)$	0	0.19	0.13	0.68
	142	166	213	T(MgII, z)	0	0.08	0.27	0.65
$\Gamma_4(B_{2g})$	418	396	517	$R(SiO_4, z)$	0	0.88	0.11	0.01
	318	316	367	T(MgII, y)	0	0.46	0.13	0.41
	260	276	321	T(MgII, SiO_4, x)	0	0.42	0.06	0.52
	224	230	264	T(MgII, SiO_4, x)	0	0.15	0.85	0
	192	180	223	T(MgII, SiO_4, y)	0	0.12	0.83	0.05
$\Gamma_3(B_{3g})$	376	367	382	$R(SiO_4, z)$	0	0.31	0.05	0.64
	318	304	328	$R(SiO_4, y)$	0	0.25	0.47	0.28
	272	277	256	$T(SiO_4, z)$	0	0.10	0.24	0.66
	226	234	174	$T(SiO_4, z)$	0	0.34	0.25	0.41

[a] T and R represent translational and rotational components respectively

most of the modes the agreement with the Raman data is within 10 percent.

For the representations Γ_6, Γ_7 and Γ_8, there is a macroscopic electric field associated with certain vibrations which give rise to the LO−TO splitting. We have used the approach given by Rao et al. (1985a), to classify the LO and TO modes belonging to these representations. From the group theoretical symmetry vectors or the calculated polarisation vectors, one notices that the atomic vibrations occur purely along the unique axis $\boldsymbol{b}^*$ for the modes of the Γ_8 representation, whereas the atomic vibrations may occur along any direction in the $\boldsymbol{a}^*\boldsymbol{c}^*$ plane for the Γ_6 and Γ_7 representations. Clearly for the Γ_8 representation, the LO and TO modes are obtained for wavevectors ($q>0$) along the $\boldsymbol{b}^*$ axis and perpendicular to the $\boldsymbol{b}^*$ axis (in the $\boldsymbol{a}^*-\boldsymbol{c}^*$ plane) respectively. On the other hand, for the Γ_6 representation, even though the atomic vibrations may occur along any direction in the $\boldsymbol{a}^*-\boldsymbol{c}^*$ plane, it can be shown that the macroscopic field can occur only along the $\boldsymbol{a}^*$ axis. Therefore, the LO and TO modes for the Γ_6 representation are obtained for wavevectors ($q>0$) along the $\boldsymbol{a}^*$ axis and perpendicular to it, respectively. Similarly, for the Γ_7 representation, the macroscopic field can occur only along the $\boldsymbol{c}^*$ axis. Therefore, the LO and TO modes for the Γ_7 representation are obtained for wavevectors ($q>0$) along the $\boldsymbol{c}^*$-axis and perpendicular to the $\boldsymbol{c}^*$ axis, respectively.

In Table 7 we have compared our calculated LO and TO mode frequencies with experimental data. For many of these modes, the eigenvectors are different linear combinations of symmetry vectors, making it difficult to assign its corresponding TO counterpart for a given LO mode. For example, the highest 618 cm^{-1} LO mode in the $B_{2u}(\Gamma_8)$ representation may seem to correspond to the 414 cm^{-1} TO mode; however their eigenvectors are entirely different. Whereas the 618 cm^{-1} (LO) mode corresponds to translations of both the magnesium atoms and the [SiO_4] group, the 414 cm^{-1} has a significant rotational component of the SiO_4 group in addition to the first magnesium atom translations.

For the sake of completeness, we have included Iishi's (1978) calculated $q\approx 0$ frequencies and eigenvector assignments in Tables 6 and 7. It can be seen that his eigenvectors are very different from ours and this difference stems from the differences in the models considered. It should be pointed out that the same eigenvector assignments have been given by Iishi (1978) for the LO and TO modes even when the LO and TO frequencies differ appreciably. Table 8 shows a comparison of neutron data at $q=0$ with Raman and infrared results.

6.5. *Specific Heat*

The phonon density of states $g(\omega)$ was used to compute the specific heat C_v given by

$$C_v=\frac{d}{dT}\left\{\int\left(n+\frac{1}{2}\right)g(\omega)\,\hbar\omega\,d\omega\right\}. \tag{14}$$

Table 7. Polar long-wavelength modes in Mg_2SiO_4; phonon frequencies in cm^{-1}

Repn.	Exptl.		Iishi (1978)			This work-external modes only									
	ω		ω		Eigenvector	ω	Eigenvector[2] [a]				ω	Eigenvector[2] [a]			
	LO	TO	LO	TO		LO	MgI T	MgII T	SiO_4 T	SiO_4 R	TO	MgI T	MgII T	SiO_4 T	SiO_4 R
$\Gamma_7(B_{1u})$	994	885	913	890	v_3										
	585	502	540	492	v_4										
	489	483	491	480	v_2										
	459	423	420	417	$R(SiO_4, y)$	618	0.32	0.34	0.34	0	414	0.34	0.09	0.02	0.55
	371	365	362	345	$R(SiO_4, z)$	413	0.28	0.13	0	0.59	389	0.47	0.13	0.22	0.18
	318	296	343	309	T(MgI, y)	339	0.36	0.18	0	0.46	323	0.15	0.34	0.06	0.45
	278	274	274	266	T(MgI, y; MgII, z)	300	0.62	0.01	0.01	0.36	293	0.75	0.04	0.02	0.19
		224	231	230	T(MgI, x)	279	0.77	0.02	0	0.21	276	0.56	0.13	0.01	0.30
		201	209	208	T(MgI, y, z)	204	0.44	0.16	0.02	0.38	202	0.50	0.12	0.02	0.36
$\Gamma_8(B_{2u})$	993	987	958	957	v_3										
	979	882	917	897	v_3										
	843	838	833	833	v_1										
	597	537	584	581	v_4										
	516	510	560	543	v_4										
	493	465	513	467	v_2										
	426	421	423	417	$R(SiO_4, z)$	624	0.38	0.27	0.35	0	562	0.73	0.13	0.13	0.01
	412	400	359	357	T(MgI, z)	561	0.70	0.15	0	0.15	485	0.80	0	0.19	0.01
	376	352	344	321	T(MgII, x, y)	480	0.80	0.01	0.16	0.03	408	0.24	0.34	0.06	0.36
	313	294	312	314	T(MgI, x, z; MgII, z)	403	0.05	0.42	0.01	0.52	381	0.60	0.09	0.20	0.11
	283	280	297	278	T(MgI, y)	332	0.46	0.53	0	0.01	312	0.10	0.81	0.09	0
		224	238	235	T(MgII, x)	267	0.08	0.46	0.02	0.44	267	0.08	0.46	0.02	0.44
		201	140	139	T(MgI, x, SiO_4, x)	194	0.34	0	0.64	0.02	193	0.34	0.01	0.64	0.01
$\Gamma_6(B_{3u})$	1086	980	976	956	v_3										
	963	957	916	915	v_3										
	845	838	827	826	v_1										
	645	601	601	565	v_4										
	566	562	527	527	v_4										
	544	498	494	493	v_2										
	469	403	413	403	$R(SiO_4, x)$	601	0.18	0.48	0.34	0	531	0.85	0.08	0	0.07
	386	378	392	363	T(MgI, z)	531	0.85	0.08	0	0.07	457	0.39	0.50	0.10	0.01
	323	320	347	312	T(MgI, y, z)	441	0.72	0.20	0.02	0.06	416	0.59	0.28	0.13	0
	298	293	309	303	T(MgI, x, z)	414	0.63	0.26	0.10	0.01	364	0.27	0.03	0.03	0.67
	276	274	265	264	T(MgI, x; MgII, y)	356	0.09	0.07	0	0.84	321	0.08	0.50	0.17	0.25
		224	242	238	T(MgI, x, y)	315	0.04	0.78	0.18	0	300	0.31	0.32	0.23	0.08
		201	190	188	T(MgI, SiO_4, y)	135	0.27	0.04	0.67	0.02	132	0.27	0.04	0.67	0.02

[a] T and R represent translational and rotational components respectively

Table 8. Comparison of zone centre phonons (in cm^{-1}) measured by Inelastic Neutron Scattering (INS), Raman and Infrared (IR) techniques

INS	Raman[a]	IR[a]
104	–	–
144	142	144
184	183	–
192	192	–
200	–	201
258	260	–
315	318	313
325	324	323

[a] Raman and IR data from Iishi (1978)

Figure 9a shows a comparison of the measured specific heat data up to 380 K (Robie et al. 1982) and the computed specific heat as a function of temperature using the density of states corresponding to the rigid molecular-ion model. In the low temperature region (between 0–100 K), the computed and experimental data agree to within 1 percent. However, the discrepancy between the two increases with increasing temperature. This is because in this model the internal modes representing Si–O and O–O vibrations are not taken into account; these high frequency modes give significant contributions only at high temperatures. Therefore, this model is able to predict the specific heat in agreement with experiment only at low temperatures. Since all the degrees of freedom are not accounted for, the Dulong-Petit value of specific heat at high temperatures

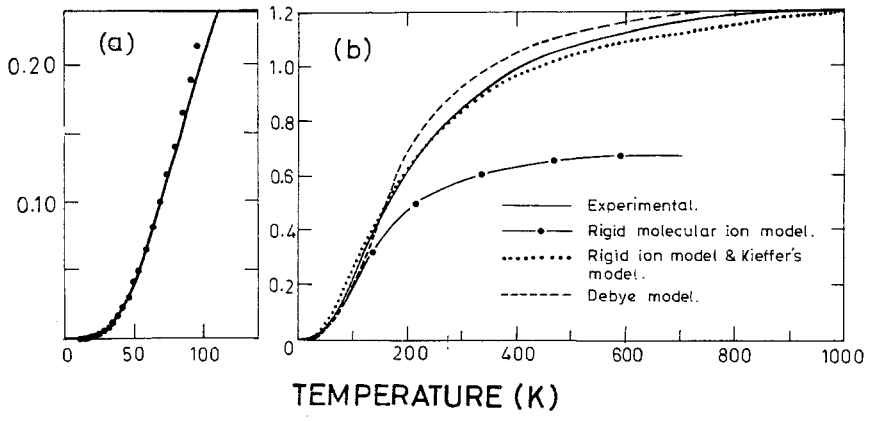

Fig. 9a, b. Comparison of experimental specific heat data with theoretical results. (**a**) low temperature region showing comparison of theoretical results given by the rigid molecular-ion model (continuous line) with the experimental data shown by the filled circles. No fitting is attempted. (**b**) Comparison of experimental data (continuous line) with results of various theoretical models as indicated in the figure. The discrepancy between the results of the rigid molecular-ion model and those from experiment is due to consideration of only external modes in this model. The difference between the results of the rigid ion model and those from experiment at high temperatures can be accounted for by anharmonic contributions (Narayani Choudhury et al. 1988)

is different for the calculated and experimental results. In the rigid ion model, where all degrees of freedom are taken into account, the agreement between computed and experimental specific heat (Robie et al. 1982, Stull and Prophet 1971) is satisfactory at all temperatures as shown in Figure 9b. The specific heat of olivine reaches its Dulong-Petit value (0.125 J/gm K) only at temperatures above 1800 K (Encyclopaedia Britannica (1980)).

In theories of specific heat, it is customary to test the applicability of the Debye model. Usually one fits a Debye curve to the experimental specific heat and calculates the Debye temperature as a function of temperature. If the Debye model were strictly valid, the Debye temperature would be independent of temperature. Considerable variations of the Debye temperature with temperature (Kieffer 1985) and also from the values of the Debye temperature obtained from elastic constants data (Kieffer 1985) indicate that the Debye model is inadequate to give the details of specific heat. In Figure 9b we show the specific heat as given by the Debye model corresponding to the Debye temperature as obtained from the observed elastic constants. Kieffer (1985) has proposed an alternative empirical model for the frequency distribution based on spectroscopic considerations, accounting for the dispersion of only the low-frequency modes. In this model, the acoustic modes are assumed to have a sinusoidal dispersion and all the optic modes, except the lowest frequency optic mode, are replaced by dispersionless Einstein frequencies. It is assumed that the lowest frequency optic mode decreases monotonically in frequency across the zone. Such a model for forsterite is found to predict the thermodynamic properties quite well and the computed specific heat is found to be very close to that obtained from our rigid ion calculations. Robie et al. (1982) have combined their heat capacity data between 300 K and 380 K with the heat content data of Orr (1953) between 398.1 K and 1807.6 K to generate values for the molar heat capacity function in the temperature range 298 K to 1800 K. This specific heat function compares well with our computed values.

7. Summary

In this paper we have reported results of a theoretical and experimental study of the dynamics of crystalline $\alpha-Mg_2SiO_4$. Detailed lattice dynamical studies based on the rigid molecular-ion model and the rigid ion model have been carried out using interatomic pair potentials involving Coulombic, short-range and covalent contributions. The parameters of the potential have been obtained on the basis of x-ray diffraction results. Elastic constants and specific heat have been computed and compared with the corresponding experimental data. Phonon dispersion relation derived along the three high-symmetry directions in the Brillouin zone have been used to obtain one-phonon coherent neutron inelastic scattering cross-sections from a single crystal for planning neutron inelastic scattering experiments. Partial and total phonon densities of states have been derived and used to evaluate the inelastic neutron scattering from a powder after taking into account multiphonon contributions. Coherent neutron inelastic scattering techniques have been employed to measure the neutron intensity distribution from a powder as well as the phonon dispersion relation from a single crystal. These are the first inelastic neutron scattering results on Mg_2SiO_4. The experimental results are in excellent agreement with the results of the model calculations within the experimental error limits and theoretical approximations. We believe that the potential formulation used in these studies can be used for deriving physical properties of forsterite at high temperatures and pressures as well as other phases of Mg_2SiO_4.

Acknowledgements. We gratefully acknowledge kind encouragement from Dr. P.K. Iyengar, Director, BARC. We are greatly indebted to Prof. Takei, University of Tokyo, Japan, for the forsterite single crystal and to Chan Han, University of Washington, for the synthesis of the Mg_2SiO_4 powder sample. This research has been supported by the NSF grant EAR-8417767(S.G.) and by the Division of Materials Sciences, U.S. Department of Energy under contracts no. DE-AC 2-76CH 00016 (J.M.H. and L.M.C.) and W-31-109-ENG-38(D.L.P.).

Appendix

Group Theoretical Symmetry Vectors $\xi(n)$ of External Modes of Mg_2SiO_4, $n=1$ through 48. $x(K)$, $y(K)$, $z(K)$ and $\theta_x(K)$, $\theta_y(K)$ and $\theta_z(K)$ are the unit vectors along the translational and rotational coordinates. $K=1, 2 \ldots 12$ correspond to the atomic/molecular labelling given in Table 1. The coordinate axes are along the cell axes ***a***, ***b*** and ***c***.

(a) *Symmetry vectors along* Σ *direction*

$\Sigma = 13\Sigma_1 + 11\Sigma_2 + 13\Sigma_3 + 11\Sigma_4$

(i) Σ_1 *representation*

$\Sigma(1) = x(1) + x(2) + x(3) + x(4);$
$\Sigma(2) = y(1) - y(2) - y(3) + y(4);$
$\Sigma(3) = z(1) - z(2) + z(3) - z(4);$
$\Sigma(4) = x(5) + x(6);$
$\Sigma(5) = z(5) - z(6);$
$\Sigma(6) = x(7) + x(8);$
$\Sigma(7) = z(7) - z(8);$
$\Sigma(8) = x(9) + x(10);$
$\Sigma(9) = z(9) - z(10);$
$\Sigma(10) = x(11) + x(12);$
$\Sigma(11) = z(11) - z(12);$
$\Sigma(12) = \theta_y(9) - \theta_y(10);$
$\Sigma(13) = \theta_y(11) - \theta_y(12).$

(ii) Σ_2 *representation*

$\Sigma(14) = x(1) + x(2) - x(3) - x(4);$
$\Sigma(15) = y(1) - y(2) + y(3) - y(4);$
$\Sigma(16) = z(1) - z(2) - z(3) + z(4);$
$\Sigma(17) = y(5) - y(6);$
$\Sigma(18) = y(7) - y(8);$
$\Sigma(19) = y(9) - y(10);$
$\Sigma(20) = y(11) - y(12);$
$\Sigma(21) = \theta_x(9) + \theta_x(10);$
$\Sigma(22) = \theta_z(9) - \theta_z(10);$
$\Sigma(23) = \theta_x(11) + \theta_x(12);$
$\Sigma(24) = \theta_z(11) - \theta_z(12).$

(iii) Σ_3 *representation*

$\Sigma(25) = x(1) - x(2) + x(3) - x(4);$
$\Sigma(26) = y(1) + y(2) - y(3) - y(4);$
$\Sigma(27) = z(1) + z(2) + z(3) + z(4);$
$\Sigma(28) = x(5) - x(6);$
$\Sigma(29) = z(5) + z(6);$
$\Sigma(30) = x(7) - x(8);$
$\Sigma(31) = z(7) + z(8);$
$\Sigma(32) = x(9) - x(10);$
$\Sigma(33) = z(9) + z(10);$
$\Sigma(34) = x(11) - x(12);$
$\Sigma(35) = z(11) + z(12);$
$\Sigma(36) = \theta_y(9) + \theta_y(10);$
$\Sigma(37) = \theta_y(11) + \theta_y(12).$

(iv) Σ_4 *representation*

$\Sigma(38) = x(1) - x(2) - x(3) + x(4);$
$\Sigma(39) = y(1) + y(2) + y(3) + y(4);$
$\Sigma(40) = z(1) + z(2) - z(3) - z(4);$
$\Sigma(41) = y(5) + y(6);$
$\Sigma(42) = y(7) + y(8);$
$\Sigma(43) = y(9) + y(10);$
$\Sigma(44) = y(11) + y(12);$
$\Sigma(45) = \theta_x(9) - \theta_x(10);$
$\Sigma(46) = \theta_z(9) + \theta_z(10);$
$\Sigma(47) = \theta_x(11) - \theta_x(12);$
$\Sigma(48) = \theta_z(11) + \theta_z(12).$

(b) *Symmetry Vectors for* Δ *direction*

$\Delta = 12\Delta_1 + 12\Delta_2 + 12\Delta_3 + 12\Delta_4.$

(i) Δ_1 *representation*

$\Delta(1) = x(1) - x(2) - x(3) + x(4);$
$\Delta(2) = y(1) + y(2) + y(3) + y(4);$
$\Delta(3) = z(1) + z(2) + z(3) + z(4);$
$\Delta(4) = x(5) + x(6) - x(7) - x(8);$
$\Delta(5) = y(5) + y(6) + y(7) + y(8);$
$\Delta(6) = z(5) - z(6) - z(7) + z(8);$
$\Delta(7) = x(9) + x(10) - x(11) - x(12);$
$\Delta(8) = y(9) + y(10) + y(11) + y(12);$
$\Delta(9) = z(9) - z(10) - z(11) + z(12);$
$\Delta(10) = \theta_x(9) - \theta_x(10) - \theta_x(11) + \theta_x(12);$
$\Delta(11) = \theta_y(9) - \theta_y(10) + \theta_y(11) - \theta_y(12);$
$\Delta(12) = \theta_z(9) + \theta_z(10) + \theta_z(11) + \theta_z(12);$

(ii) Δ_2 *representation*

$\Delta(13) = x(1) + x(2) - x(3) - x(4);$
$\Delta(14) = y(1) - y(2) + y(3) - y(4);$
$\Delta(15) = z(1) - z(2) - z(3) + z(4);$
$\Delta(16) = x(5) - x(6) - x(7) + x(8);$
$\Delta(17) = y(5) - y(6) + y(7) - y(8);$
$\Delta(18) = z(5) + z(6) - z(7) - z(8);$
$\Delta(19) = x(9) - x(10) - x(11) + x(12);$
$\Delta(20) = y(9) - y(10) + y(11) - y(12);$
$\Delta(21) = z(9) + z(10) - z(11) - z(12);$
$\Delta(22) = \theta_x(9) + \theta_x(10) - \theta_x(11) - \theta_x(12);$
$\Delta(23) = \theta_y(9) + \theta_y(10) + \theta_y(11) + \theta_y(12);$
$\Delta(24) = \theta_z(9) - \theta_z(10) - \theta_z(11) + \theta_z(12).$

(iii) Δ_3 *representation*

$\Delta(25) = x(1) - x(2) + x(3) - x(4);$
$\Delta(26) = y(1) - y(2) - y(3) - y(4);$
$\Delta(27) = z(1) + z(2) + z(3) + z(4);$
$\Delta(28) = x(5) - x(6) + x(7) - x(8);$
$\Delta(29) = y(5) - y(6) - y(7) + y(8);$
$\Delta(30) = z(5) + z(6) + z(7) + z(8);$
$\Delta(31) = x(9) - x(10) + x(11) - x(12);$
$\Delta(32) = y(9) - y(10) - y(11) + y(12);$
$\Delta(33) = z(9) + z(10) + z(11) + z(12);$
$\Delta(34) = \theta_x(9) + \theta_x(10) + \theta_x(11) + \theta_x(12);$
$\Delta(35) = \theta_y(9) + \theta_y(10) - \theta_y(11) - \theta_y(12);$
$\Delta(36) = \theta_z(9) - \theta_z(10) + \theta_z(11) - \theta_z(12).$

(iv) Δ_4 *representation*

$\Delta(37) = x(1) + x(2) + x(3) + x(4);$
$\Delta(38) = y(1) - y(2) - y(3) + y(4);$
$\Delta(39) = z(1) - z(2) + z(3) - z(4);$
$\Delta(40) = x(5) + x(6) + x(7) + x(8);$
$\Delta(41) = y(5) + y(6) - y(7) - y(8);$
$\Delta(42) = z(5) - z(6) + z(7) - z(8);$
$\Delta(43) = x(9) + x(10) + x(11) + x(12);$
$\Delta(44) = y(9) + y(10) - y(11) - y(12);$
$\Delta(45) = z(9) - z(10) + z(11) - z(12);$
$\Delta(46) = \theta_x(9) - \theta_x(10) + \theta_x(11) - \theta_x(12);$
$\Delta(47) = \theta_y(9) - \theta_y(10) - \theta_y(11) + \theta_y(12);$
$\Delta(48) = \theta_z(9) + \theta_z(10) + \theta_z(11) + \theta_z(12).$

(c) *Symmetry Vectors along* Λ *direction*

$\Lambda = 13\Lambda_1 + 11\Lambda_2 + 11\Lambda_3 + 13\Lambda_4.$

(i) Λ_1 *representation*

$\Lambda(1) = x(1) - x(2) + x(3) - x(4);$
$\Lambda(2) = y(1) + y(2) - y(3) - y(4);$
$\Lambda(3) = z(1) + z(2) + z(3) + z(4);$
$\Lambda(4) = x(5) - x(8);$
$\Lambda(5) = z(5) + z(8);$
$\Lambda(6) = x(6) - x(7);$
$\Lambda(7) = z(6) + z(7);$
$\Lambda(8) = x(9) - x(12);$
$\Lambda(9) = z(9) + z(12);$
$\Lambda(10) = x(10) - x(11);$
$\Lambda(11) = z(10) + z(11);$
$\Lambda(12) = \theta_y(9) - \theta_y(12);$
$\Lambda(13) = \theta_y(10) - \theta_y(11).$

(ii) Λ_2 *representation*

$\Lambda(14) = x(1) + x(2) - x(3) - x(4);$
$\Lambda(15) = y(1) - y(2) + y(3) - y(4);$
$\Lambda(16) = z(1) - z(2) - z(3) + z(4);$
$\Lambda(17) = y(5) - y(8);$
$\Lambda(18) = y(6) - y(7);$

$A(19) = y(9) - y(12)$;
$A(20) = \theta_x(9) - \theta_x(12)$;
$A(21) = \theta_z(9) + \theta_z(12)$;
$A(22) = y(10) - y(11)$;
$A(23) = \theta_x(10) - \theta_x(11)$;
$A(24) = \theta_z(10) + \theta_z(11)$.

(iii) A_3 *representation*

$A(25) = x(1) - x(2) - x(3) + x(4)$;
$A(26) = y(1) + y(2) + y(3) + y(4)$;
$A(27) = z(1) + z(2) - z(3) - z(4)$;
$A(28) = y(5) + y(8)$;
$A(29) = y(6) + y(7)$;
$A(30) = y(9) + y(12)$;
$A(31) = \theta_x(9) + \theta_x(12)$;
$A(32) = \theta_z(9) - \theta_z(12)$;
$A(33) = y(10) + y(11)$;
$A(34) = \theta_x(10) + \theta_x(11)$;
$A(35) = \theta_z(10) - \theta_z(11)$.

(iv) A_4 *representation*

$A(36) = x(1) + x(2) + x(3) + x(4)$;
$A(37) = y(1) - y(2) - y(3) + y(4)$;
$A(38) = z(1) - z(2) + z(3) - z(4)$;
$A(39) = x(5) + x(8)$;
$A(40) = z(5) - z(8)$;
$A(41) = x(6) + x(7)$;
$A(42) = z(6) - z(7)$;
$A(43) = x(9) + x(12)$;
$A(44) = z(9) - z(12)$;
$A(45) = \theta_y(9) + \theta_y(12)$;
$A(46) = x(10) + x(11)$;
$A(47) = z(10) - z(11)$;
$A(48) = \theta_y(10) + \theta_y(11)$.

References

Beeson JM, Pinceaux JP, Anastopoulos C (1982) Raman spectra of olivine up to 65 kilobars. Geophys Res 87:773–775

Born M, Huang K (1954) The dynamical theory of crystal lattices. Clarendon Press, Oxford

Brüesch P (1982) Phonons: Theory and experiments I. Springer, Berlin Heidelberg New York

Carpenter JM, Price DL (1985) Correlated motions in glasses studied by coherent inelastic neutron scattering. Phys Rev Letters 54:441–443

Chaplot SL (1978) A computer program for external modes in complex molecular-ionic crystals. Report B.A.R.C.-972, Bhabha Atomic Research Centre, Bombay, India

Chaplot SL, Rao KR, Roy AP (1984) Phonon dispersion relation in $LiKSO_4$. Phys Rev B29:4747–4756

Cygan RT, Lasaga AC (1986) Dielectric and polarization behavior of forsterite at elevated temperatures. Am Mineral 71:758–766

Derighetti B, Hafner S, Marxer H, Rager H (1978) NMR of ^{29}Si and ^{25}Mg in Mg_2SiO_4 with dynamic polarisation technique. Phys Letters 66A:150–152

Encyclopaedia Britanica (1980) (Encyclopaedia Britanica Inc, Chicago, London etc.), 15th edition, p 960

Fujino K, Sasaki S, Takeuchi Y, Sadanaga R (1981) X-ray determination of electron distributions in forsterite, fayalite and tephroite. Acta Crystallogr B37:513–518

Ghose S, Hastings JM, Corliss LM, Rao KR, Chaplot SL, Choudhury N (1987) Study of phonon dispersion relation in forsterite, Mg_2SiO_4 by inelastic neutron scattering. Solid State Commun 63:1045–1050

Graham EK Jr, Barsch GR (1969) Elastic constants of single crystal forsterite as a function of temperature and pressure. J Geophys Res 74:5949–5960

Hofmeister AM (1987) Single crystal absorption and reflection infrared spectroscopy of forsterite and fayalite. Phys Chem Minerals 14:499–513

Iishi K (1978) Lattice dynamics of forsterite. Am Mineral 63:1198–1208

International tables for X-ray crystallography (1952) Published for the International Union of Crystallography by Kynoch Press, V.I.

Jeanloz R (1980) Infrared spectra of olivine polymorphs: α, β-phase and spinel. Phys Chem Minerals 5:327–339

Kieffer SW (1985) Heat capacity and entropy; systematic relations to lattice vibrations. Rev Mineralogy 15:65–126

Kudoh Y, Takeuchi Y (1985) The crystal structure of forsterite under high pressure upto 140 kbar. Z Kristallogr 171:291–302

Kumazawa M, Anderson OL (1969) Elastic modulii, pressure derivatives and temperature derivaties of single crystal olivine and single crystal forsterite. J Geophys Res 74:5961–5972

Maradudin AA, Vosko SH (1968) Symmetry properties of the normal vibrations of a crystal. Rev Mod Phys 40:1–37

Matsui M, Matsumoto T (1982) An interatomic potential function model for Mg, Ca and Ca–Mg olivines. Acta Crystallogr A38:513–515

Matsui M, Busing WR (1984) Computational modelling of the structure and elastic constants of the olivine and spinel forms of Mg_2SiO_4. Phys Chem Minerals 11:55–59

McLarnan TR, Hill RJ, Gibbs GV (1979) A CNDO/2 molecular orbital study of shared tetrahedral comformations in olivine type compounds. Aust J Chem 32:949–959

Narayani Chaudhury, Chaplot SL, Rao KR (1988) Thermal expansion, equation of state and melting point studies of forsterite, α-Mg_2SiO_4. (submitted to Physics and Chemistry of Minerals)

Oehler O, Günthard HH (1969) Low temperature infrared spectra between 1200 and 20 cm^{-1} and normal coordinate analysis of silicates with olivine structures. J Chem Phys 51:4719–4728

Orr RL (1953) High temperature heat contents of magnesium orthosilicates and ferrous orthosilicates. J Am Chem Soc 75:528–529

Paques-Ladent, Tarte P (1973) Vibrational studies of olivine-type compounds-I; The IR and Raman spectra of the isotopic species of Mg_2SiO_4. Spectrochem Acta 29A:1007–1016

Price DL (1982) Unpublished information

Price GD, Parker SC (1984) Computer simulations of the structural and physical properties of the olivine and spinel polymorphs of Mg_2SiO_4. Phys Chem Minerals 10:209–216

Price GD, Parker SC, Leslie M (1987) The lattice dynamics of forsterite. Mineral Mag 51:157–170

Rao KR, Chaplot SL, Iyengar PK, Venkatesh AH, Vijayaraghavan PR (1978) Inelastic neutron scattering from and lattice dynamics of α-KNO_3. Pramana (J Phys) 11:251–288

Rao KR, Chaplot SL, Padmanabhan VM, Vijayaraghavan PR (1982) Neutron, X-ray, and lattice dynamical studies of paraelectric Sb_2S_3. Pramana (J Phys) 19:593–632

Rao KR, Chaplot SL (1985a) Dynamics of paraelectric and ferroelectric SbSI. Physica Status Solidi (b) 129:471

Rao KR, Chaplot SL, Choudhury N, Ghose S (1985b) Lattice dynamics of forsterite, Mg_2SiO_4. In: Phonon Physics. Kollar J, Kroo N, Menyhard N, Siklos T (Ed) World Scientific Co., Singapore, p 171–174

Rao KR, Chaplot SL (1985c) Lattice dynamics of complex ionic crystals. In: Phonon Physics. Kollar J, Kroo N, Menyhard N, Siklos T (Ed) World Scientific Co., Singapore, p 175–178

Rao KR, Chaplot SL, Choudhury N, Ghose S, Price DL (1987) Phonon density of states and specific heat of forsterite, Mg_2SiO_4. Science 236:64

Robie RA, Hemingway BS (1982) Heat capacities and entropies of Mg_2SiO_4, Mn_2SiO_4 and Co_2SiO_4 between 5 and 380 K. Am Mineral 67:470–482

Sasaki S, Fujino K, Takéuchi Y, Sadanaga R (1980) On the estimation of atomic charge by the x-ray method for some oxides and silicates. Acta Crystallogr A36:904–915

Sasaki S, Prewitt CT, Sato Y, Ito E (1982) Single crystal x-ray study of γ-Mg_2SiO_4. J Geophys Res 87:7829–7832

Servoin JL, Piriou B (1973) Infrared reflectivity and Raman scattering of Mg_2SiO_4 single crystal. Phys Status Solidi 55:677–686

Sieskind M (1978) Classification and simplifications introduced in the group of the neutral elements of crystalline sites in the lattice dynamics. Application to α-mercuric iodide. J Phys Chem Solids 39:1251–1268

Sjolander A (1958) Multiphonon processes in slow neutron scattering by crystals. Arkiv fur Fysik 14:315–371

Smyth JR, Hazen RM (1973) The crystal structures of forsterite and hortonolite at several temperatures upto 900 K. Am Mineral 58:588–593

Stull DR, Prophet H (Eds) (1971) JANAF-Thermochemical tables (second edition), U.S. Department of Commerce, National Bureau of Standards, Washington

Suzuki I, Anderson OL, Sumino Y (1983) Elastic properties of a single crystal forsterite Mg_2SiO_4 upto 1200 K. Phys Chem Minerals 10:38–46

Takeuchi Y, Yamanaka T, Haga N, Hirano M (1984) High-temperature crystallography of olivines and spinels. In: Materials Science of the Earth's Interior, Sunagawa I (Ed) Terra Scientific Publishing Co, Tokyo, 191–231

Verma RK (1960) Elasticity of some high density crystals. J Geophys Res 65:757–766

Venkataraman G, Sahni VC (1970) External vibrations in complex crystals. Rev Mod Phys 42:409–470

Venkataraman G, Feldkamp L, Sahni VC (1975) Dynamics of perfect crystals. MIT Press Cambridge

Received February 20, 1987